

# Closed-form Kinematic Model and Workspace Characterization for Magnetic Ball Chain Robots

Giovanni Pittiglio, *Member, IEEE*, Margherita Mencattelli and Pierre E. Dupont, *Fellow, IEEE*

**Abstract**—Magnetic ball chains are well suited to serve as the steerable tips of endoluminal robots. While it has been demonstrated that these robots produce a larger reachable workspace than magnetic soft continuum robots designed using either distributed or lumped magnetic material, here we investigate the orientational capabilities of these robots. To increase the range of orientations that can be produced at each point in the workspace, we introduce a comparatively-stiff outer sheath from which the steerable ball chain is extended. We present an energy-based kinematic model and also derive an approximate expression for the range of achievable orientations at each point in the workspace. Experiments are used to validate these results.

**Index Terms**—Steerable Catheters/Needles, Surgical Robotics, Magnetic Actuation.

## I. INTRODUCTION

Robots and manual instruments used for endoluminal procedures are typically constructed with a steerable tip section and a long passive flexible proximal section. Such devices include cardiac catheters, bronchoscopes, ureterscopes and bronchoscopes [1]. By pushing and rotating the proximal section while also flexing the steerable section, it is possible to navigate through branching anatomical passages and to position the instrument tip to perform clinical tasks within the anatomy.

When developing a robot for a specific endoluminal task, the steerable tip must be designed to meet the navigation and tool positioning requirements of the task [2]. One measure for considering the versatility of steerable tip designs to meet task requirements is to compare reachable workspace. This is not sufficient, however, since successfully steering into an endoluminal side branch places requirement on both tip position and orientation. Furthermore, many diagnostic and therapeutic tasks require the instrument tip to meet orientational constraints with respect to the tissue surface. Examples include targeting a subsurface lesion for biopsy or driving in a tissue anchor normal to the endoluminal surface [3].

Consequently, for comparing steerable tip designs, dexterous workspace, comprised of the set of tip positions that can be reached from any possible direction, is an appropriate metric. The challenge, however, is that these robot designs produce bugle-shaped workspaces. They typically do not

The authors are with the Department of Cardiovascular Surgery, Boston Children's Hospital, Harvard Medical School, Boston, MA 02115, USA. Email: {giovanni.pittiglio, margherita.mencattelli, pierre.dupont}@childrens.harvard.edu  
 This work was supported by the National Institutes of Health under grant R01HL124020.

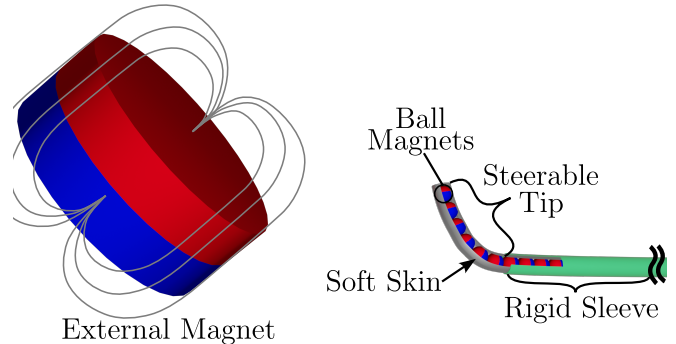


Fig. 1: Magnetic ball chain robot as the steerable tip of an interventional system.

possess a classically-defined dexterous workspace since they cannot achieve an arbitrary tip orientation at any point in their reachable workspace [1].

Nevertheless, it is of great value during the design process to be able to characterize the range of orientations that a steerable tip can achieve at each position in its workspace. This is a computationally intensive process, however, since most designs are continuum robots whose kinematics are described by differential equations in arc length with boundary conditions split between the proximal and distal ends.

In this paper, we present a magnetically-actuated steerable tip design (see Fig. 1) that possesses both a large reachable workspace [4] and a large range of tip orientations at each position in the reachable workspace, as schematically represented in Fig. 2. While the physics-based kinematic model is posed as an energy minimization problem and so is computationally intensive, we also derive an approximate expression for the achievable orientation range at each tip position that can be easily calculated. This modeling framework facilitates the design process while also providing an accurate model for kinematic control.

The remainder of the paper is arranged as follows. The next section presents the magnetic ball chain design and presents the physics-based kinematic model. Section III derives the simplified workspace characterization. Experiments validating the kinematic model and workspace are presented in Section IV. Conclusions are given in Section V.

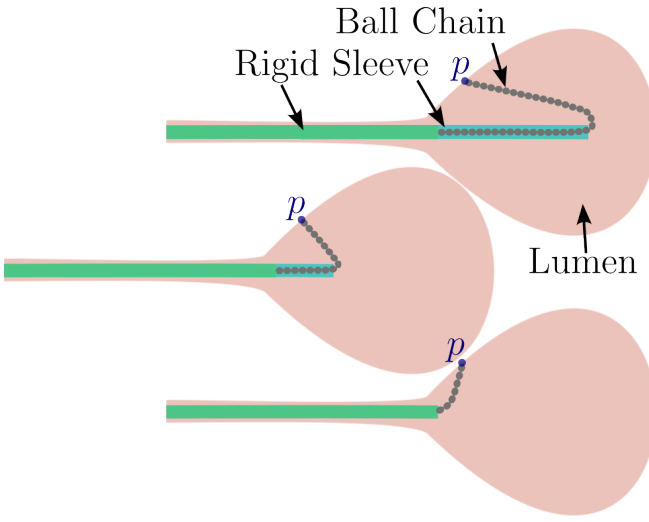


Fig. 2: Adding a retractable sleeve to the ball chain steerable tip enables the robot to approach a tip position,  $p$ , from multiple tangent directions.

## II. MAGNETIC BALL CHAIN ROBOTS

In magnetically-actuated robots, permanent magnetic material is embedded in the steerable tip [5], [6], [7], or along the length [8], [9], [10], [11], [12], and external magnets are used to generate forces and torques on the embedded material [11], [6], [7], [13]. This approach offers several advantages in comparison to more traditional actuation methods such as tendons [14], [15]. First, power is transmitted wirelessly to the steerable tip which simplifies the design of the proximal section. Second, magnetic actuation can lead to more stable tip positioning since forces and torques are being directly applied to the tip rather than being transmitted through the proximal tether [5].

Maximizing the workspace of a magnetically-actuated continuum robot presents a design challenge that involves determining the volume, distribution and magnetic orientation of the embedded magnetic material [12], [16]. While the magnetic force and torque applied to the tip can be increased by increasing the volume of embedded magnetic material, this also increases the flexural stiffness of the robot. This is true for both discrete embedded magnets [8], [9] and for magnetic particles distributed within a polymer [10], [11], [12].

Magnetic ball chain robots represent an approach intended to address this conflict between magnetic volume and stiffness [4]. In these robots, the steerable tip is comprised of a chain of self-assembling spherical permanent magnets encased in a thin compliant cylindrical skin (Fig. 1). This design replaces the flexural continuum steerable section with an open-chain mechanism comprised of concatenated spherical joints. The mechanism has a very high magnetic volume while also being flexurally compliant owing to the spherical joints between the balls. For typical material properties and ratios of diameter to length, it has been demonstrated that ball chain designs can bend with a smaller radius of curvature

than continuum designs with either lumped magnets or distributed magnetic particles [4].

To investigate the workspace of these robots, we make the following assumptions. First, we consider designs in which the ball chain has a maximum length and can be retracted into, and extended from, the passive proximal section as shown in Fig. 1. It is assumed that any retracted portion of the ball chain conforms to the shape of the proximal section. We also assume that the external magnet produces a uniform magnetic field on the robot. The only other external loading we consider is that due to gravity. Given these assumptions, the spheres always remain in chain form. We also assume that there is no friction between the spheres and between the spheres and the elastic sleeve. While the spheres exactly match the magnetic dipole model [17], we also assume that the external magnet can be approximated as a dipole. The deformation of the elastic sleeve is assumed to be piecewise constant curvature and any twisting is neglected.

Since we are interested only in the effects of field direction and ball chain extension only, we neglect the effects of field gradient in our analysis. Forces related to field gradients are neglected in both kinematic modelling and workspace analysis.

### A. Kinematic Modeling via Energy Minimization

Under these conditions, the equilibrium pose of the robot can be calculated as a function of the external magnetic field by minimizing an expression for the total magnetic and elastic energy of the ball chain. To simplify model presentation below, we consider only the extended portion of the steerable tip and model it as having its base fixed in a world coordinate frame, at the end of the rigid portion.

For each sphere of diameter,  $d$ , in the chain of  $n$  balls, the  $z$  axis is assumed aligned with its magnetic dipole. In a world frame,  $\{\mathbf{x}_0, \mathbf{y}_0, \mathbf{z}_0\}$ , the configuration of each sphere can be described by the position,  $\mathbf{p}_i \in \mathbb{R}^3$  and orientation,  $\mathbf{R}_i \in SO(3)$  of its body frame. Since, we assume that each ball of the chain remains in contact with the previous ball, we can reduce the number of degrees of freedom from  $6n$  to  $4n$  i.e., each ball is assumed to pivot around the previous one and rotate around its own center along the two main directions ( $x$  and  $y$ ). When we assume the first ball is fixed in rotation and translation, since treated as fixed base, we obtain  $4n - 4$  total degrees of freedom. Representation of the robot is reported in Fig. 3.

We compute the magnetic field at a point  $\mathbf{r} \in \mathbb{R}^3$  generated by a dipole located at the origin of magnetic moment  $\mathbf{m}_1 = |\mathbf{m}_1| \hat{\mathbf{m}}_1 \in \mathbb{R}^3$  using the dipole model [17]

$$\mathbf{B}(\mathbf{r}, \mathbf{m}_1) = \frac{|\mathbf{m}_1| \mu_0}{4\pi |\mathbf{r}|^3} (3\hat{\mathbf{r}}\hat{\mathbf{r}}^T - \mathbf{I}) \hat{\mathbf{m}}_1 \quad (1)$$

in which, for any vector  $\mathbf{v} \in \mathbb{R}^3$ ,  $\hat{\mathbf{v}} = \mathbf{v}/|\mathbf{v}|$ , with  $|\cdot|$  the Euclidean norm.

A dipole of moment  $\mathbf{m}_2$  in a magnetic field  $\mathbf{B}$  experiences a potential energy given by

$$U_d = -\mathbf{m}_2 \cdot \mathbf{B} \quad (2)$$

The overall potential energy is the sum of energies from each pair of balls acting on each:

$$\begin{aligned} U_b &= - \sum_{i=1}^n \sum_{j=i+1}^n \mathbf{m}_j \cdot \mathbf{B}(\mathbf{p}_j - \mathbf{p}_i, \mathbf{m}_i) \\ &= - \sum_{i=1}^n \sum_{j=i+1}^n |\mathbf{m}_j| (\mathbf{R}_j e_3) \cdot \mathbf{B}(\mathbf{p}_j - \mathbf{p}_i, |\mathbf{m}_i| (\mathbf{R}_i e_3)) \end{aligned} \quad (3)$$

Note that we use the fact that  $\mathbf{m}_i = |\mathbf{m}_i| (\mathbf{R}_i e_3)$ , to express the energy with respect to the ball chain configuration parameters:  $(\mathbf{p}_i, \mathbf{R}_i)$ ,  $i = 1, 2, \dots, n$ .

In the present work we use a cylindrical external magnet of moment  $\mathbf{m}_e$ . The magnet's configuration is represented by position and orientation  $(\mathbf{p}_e, \mathbf{R}_e)$  and its diameter  $D$  is larger than its length; we can position the magnet such that all the balls in the chain satisfy  $|\mathbf{p}_i - \mathbf{p}_e| > D$ ,  $i = 1, \dots, n$  and the dipole approximation stands, with an error less than 2% [17]. The ball chain experiences a potential energy related to the field applied by the external magnet expressed as

$$U_e = - \sum_{i=1}^n \mathbf{m}_i \cdot \mathbf{B}(\mathbf{p}_i - \mathbf{p}_e, \mathbf{m}_e) \quad (4)$$

The elastic skin is here discretized into arcs spanning the contact points between adjacent pairs of balls (Fig. 3). Consecutive balls are virtually connected by arc of a circle (constant curvature segment), of radius  $\rho_i$ , and to span an angle,  $\theta_i$ .

These variables are related to the shape parameters. Specifically,  $\theta_i$  is defined by

$$\tan(\theta_i) = \frac{(\mathbf{p}_{i+1} - \mathbf{p}_i) \times (\mathbf{p}_i - \mathbf{p}_{i-1})}{(\mathbf{p}_{i+1} - \mathbf{p}_i) \cdot (\mathbf{p}_i - \mathbf{p}_{i-1})} \quad (5)$$

and the arc length is given by

$$\rho_i = (d/2) \cot(\theta_i/2) \quad (6)$$

The expression for the elastic energy of the beam is given by

$$U = \int_0^l \frac{M^2}{2EI} ds \quad (7)$$

in which  $l$  is the length,  $M$  is the bending moment,  $E$  elastic modulus and  $I$  is the area moment of inertia for the cross section. For a beam experiencing pure bending with radius of curvature,  $\rho$ , the moment  $M$  is constant and given by

$$M = EI/\rho \quad (8)$$

We combine the preceding equations for the  $i$ th ball and, noting that the length of the segment is given by  $\rho_i \theta_i$ , we express the strain energy as

$$U_s(i) = \frac{E_i I_i \theta_i}{2\rho_i} \quad (9)$$

We assume that piecewise constant elastic modulus,  $E_i$ , and second moment of area,  $I_i$ . By summing over each ball, we express the total strain energy in the skin due to bending as

$$U_s = \frac{1}{2} \sum_{i=1}^n \frac{E_i I_i \theta_i}{\rho_i} \quad (10)$$

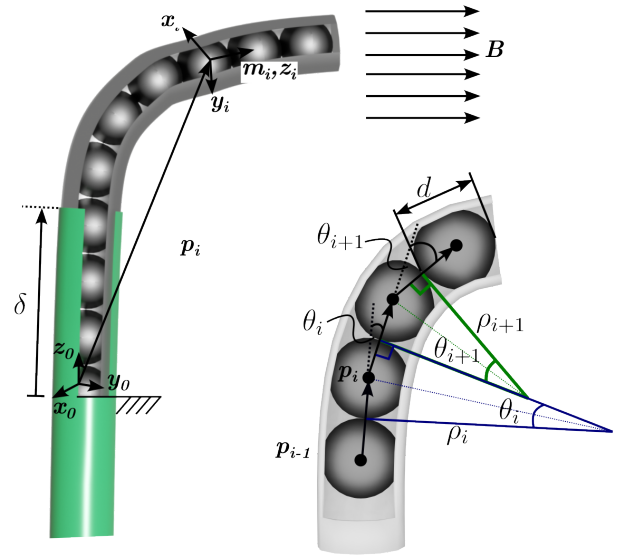


Fig. 3: Schematic of ball chain coordinate frames.

The gravitational potential energy of the ball chain is defined as the sum over the ball chain

$$U_g = \sum_{i=1}^n \mu_i \mathbf{g}^T \mathbf{p}_i, \quad (11)$$

with  $\mu_i$  as the mass of the  $i$ th ball and  $\mathbf{g}$  vector of gravitational acceleration.

The expression for total energy experienced by the ball chain,  $U$  is given by summing all the components of balls magnetic interaction, external applied field, skin elasticity and gravitational component, resulting in

$$U = U_b + U_e + U_s + U_g. \quad (12)$$

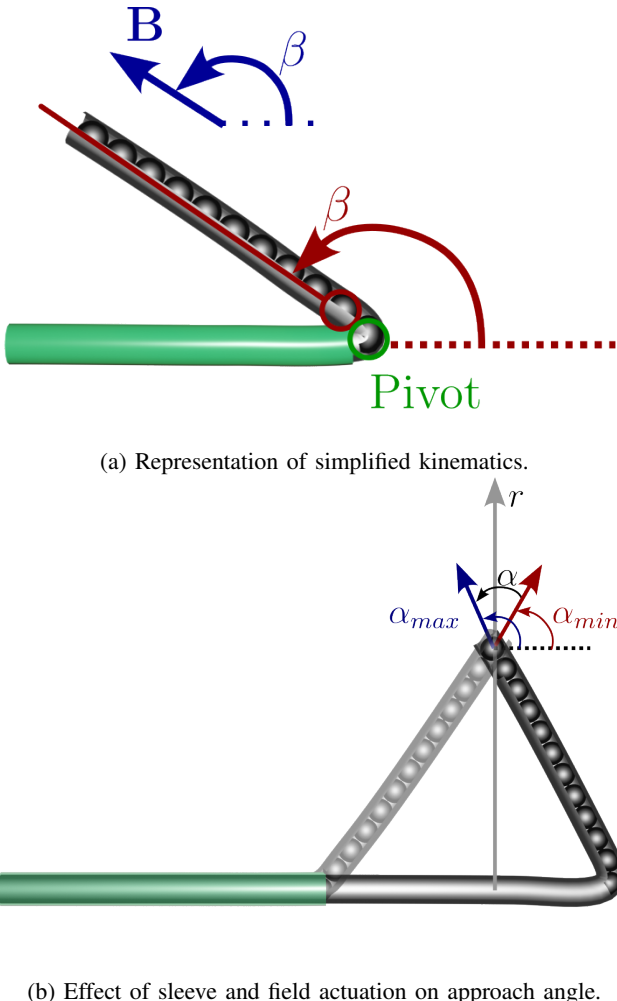
This is function of the kinematic shape parameters,  $(\mathbf{p}_i, \mathbf{R}_i)$ ,  $i \in 2, \dots, n$  and of the inputs,  $(\mathbf{p}_e, \mathbf{R}_e)$ . The solutions of the kinematics is the shape  $(\mathbf{p}_i^*, \mathbf{R}_i^*)$ ,  $i \in 2, \dots, n$ , that minimizes energy, given the input parameters i.e.,

$$(\mathbf{p}_i^*, \mathbf{R}_i^*), i \in 2, \dots, n = \arg \min_{(\mathbf{p}_i, \mathbf{R}_i), i \in 2, \dots, n} U \quad (13)$$

The minimization is solved using routines such as *fmincon* from Matlab (Mathworks, Natick, MA), where constraints result from assuming continuous contact between subsequent balls over time. Under this assumption, we impose that the distance between the balls is fixed and equal to the radius of the balls, by imposing

$$||\mathbf{p}_i|| = d \quad \forall i = 1, 2, \dots, n.$$

We also impose  $\mathbf{R}_1 = \mathbf{I}$ , with  $\mathbf{I} \in \mathbb{R}^{3 \times 3}$  identity matrix i.e., constrain the first ball to be aligned with the chain's axis. In the real setup, this is achieved by gluing.



(b) Effect of sleeve and field actuation on approach angle.

Fig. 4: Effects of high field and sleeve actuation for ball-chain magnetic robots.

### B. Approximate Workspace Characterization

While the workspace can be characterized by exhaustively evaluating the kinematic model above, this is computationally intensive and does not provide intuitive insight during the robot design process. As an alternative, a simplified model is proposed here that provides for rapid calculation of the range of tangent angles that can be achieved at a tip position.

Under the assumption that the input consists solely of the external magnetic field direction with the magnitude fixed at a sufficiently high value, e.g., higher than approx. 20 mT, we observe that when a sufficient number of balls are extended from the sheath, balls 2 to  $n$  approximately align with the field, forming a line which pivots around the first (fixed) ball (Fig. 4a). In this case, the ball chain can be approximated by a linear segment parallel to the magnetic field  $\mathbf{B}$  of a length given by  $n$  ball diameters.

Using this approximation, we can solve for the range of approach angles for any position in the workspace as shown in Fig. 4b. The limiting angles,  $\alpha_{min}$  and  $\alpha_{max}$  correspond to the two robot configurations in which the tip ball is located

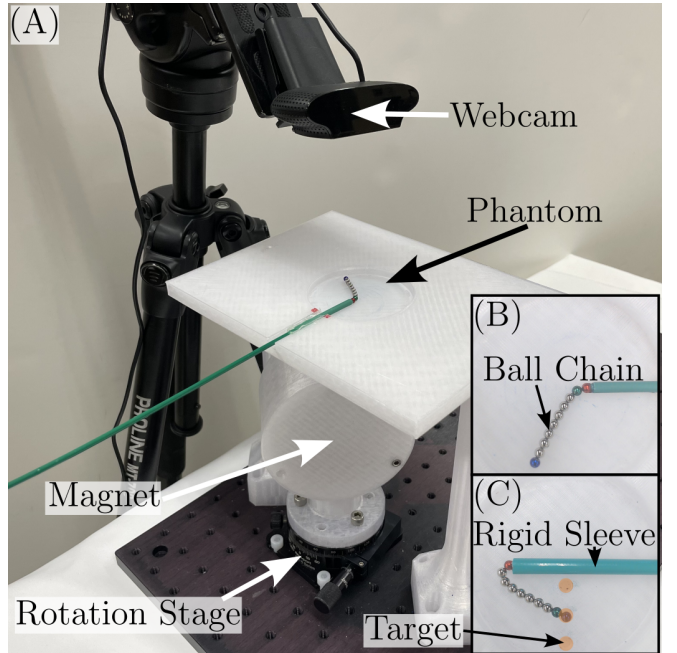


Fig. 5: Experimental setup for ball chain robot model validation. (A) Complete test system; (B) Camera view during model validation; (C) Camera view during approach angle measurements.

at the desired position with all balls extended from the sheath while the sheath slides along its axis. The range of approach angles,  $\alpha$ , is given by

$$\alpha(r) = \alpha_{max}(r) - \alpha_{min}(r) \quad (14)$$

and is a function of the perpendicular distance,  $r$ , from the robot sheath. From the figure, one can see that for  $r \rightarrow 0$  then  $\alpha \rightarrow \pi$ . Also, for  $r = nd$  then  $\alpha = 0$  with  $\alpha_{max} = \alpha_{min} = \pi/2$ .

Using the geometry shown in Fig. 4b, we can find expression for  $\alpha_{min}$  as

$$\alpha_{min}(r) = \arcsin(r/nd) \quad (15)$$

Owing to symmetry,

$$\alpha_{max}(r) = \pi - \alpha_{min}(r) = \pi - \arcsin(r/nd), \quad (16)$$

and thus,

$$\alpha(r) = \pi - 2 \arcsin(r/nd) = 2 \arccos(r/nd). \quad (17)$$

### III. EXPERIMENTS

Experiments were performed in order to validate the kinematic model of Section II and also to assess the accuracy of the workspace approach angle analysis. All experiments were performed using the setup shown in Fig. 5. The robot was composed of ten N42 magnetic spheres of diameter 3.175 mm, and remanence 1.32 T. This was the smallest strong spherical permanent magnet available commercially (K&J Magnetics, USA). Smaller and stronger custom magnets can be fabricated and used in applications which require robots with smaller diameter and higher magnetic content.

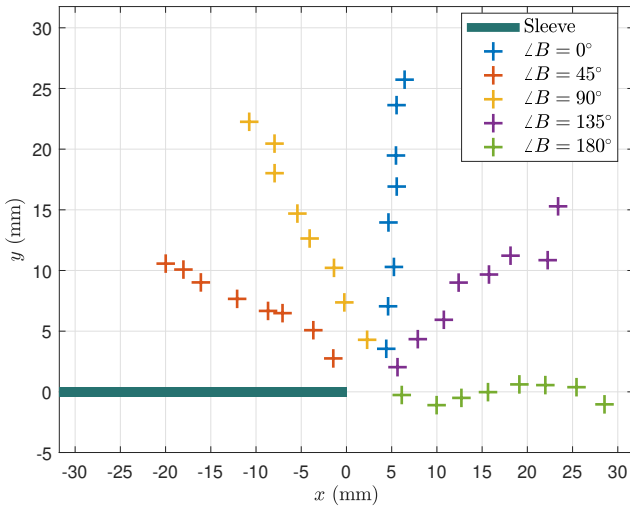


Fig. 6: Tip position of the ball chain robot extracted from image tracking for model validation experiments.

An N52 cylindrical external magnet (76.2mm diameter, 38.1mm long, 1.48 T remanence) was mounted on a single-axis rotational mechanism so that its field orientation, lying in the plane of the robot, could be precisely measured. Given the distance between the external magnet and robot, the field was approximately 23 mT for every experiment. The ball chain robot was introduced to a planar phantom which represents a generic circular anatomy of radius equal to the length of the robot,  $nd = 31.75$  mm. A webcam (C920, Logitech, US) was placed on top of the phantom so that the robot could be tracked. For tracking purposes, three balls of the chain were colored in red, green, and blue. Since its effect was observed to be negligible, we did not consider the presence of the elastic skin in our experiments.

#### A. Model Validation

To assess the accuracy of the magnetic energy kinematic model, experiments consisted of collecting tip position for magnetic field angles of 0, 45, 90, 135, 180°. For each field angle, camera images were collected for ball chains comprised of from 3 to 10 balls. The position of the first ball was used for calibration. The Matlab function *imfindcircles* was applied to each color channel to solve for the radius and center of the first and last balls. The radius information was used to convert from pixels to millimeters while the center was used to validate the model. In this experiment, no rigid sleeve was included, since we aimed at evaluating only the goodness of the model in predicting magnetic behavior. Robot extension was mimicked by sequentially adding balls at the tip. The contribution of the sleeve, while excluded here, is considered in the next section for evaluating the workspace.

Figure 6 represents the robot chain tip position extracted from the images. This data was used to validate the magnetic model, in terms of tip position. We found that the error in predicting the tip position is  $1.99 \pm 1.33$  mm i.e.,  $6.25 \pm$

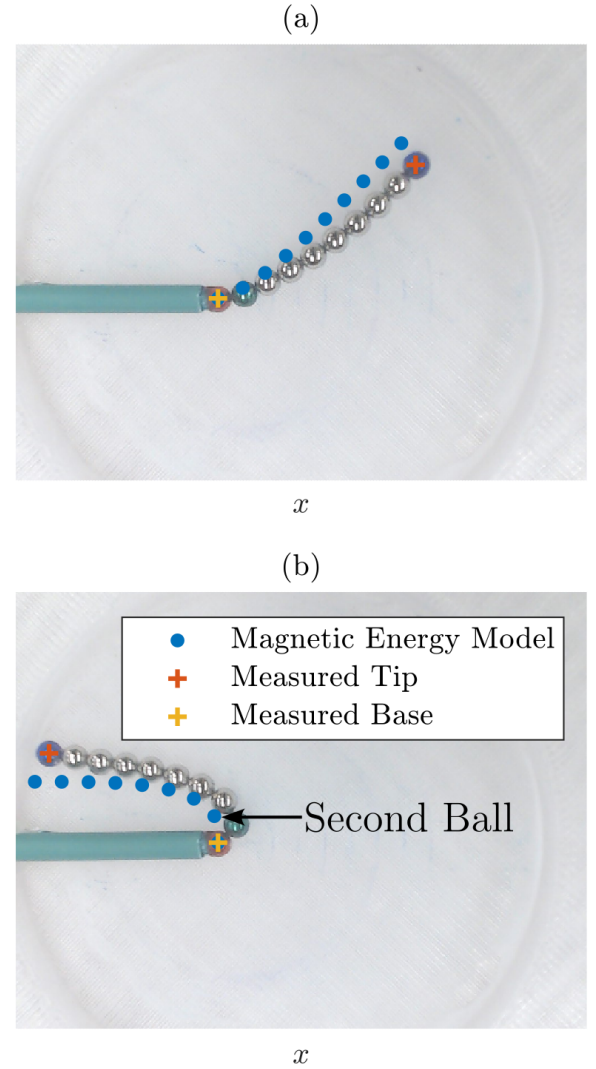


Fig. 7: Example configurations showing modeling error arising from predicted contact angles between proximal pairs of balls. (a) Example for  $\angle B = 45^\circ$ ; (b) Example for  $\angle B = 180^\circ$ .

4.20% of the robot's length, with maximum error of 5.90 mm (18.6% of the length).

In comparing the shapes of the experimental and model-predicted robot configurations, we noticed that the main source of error appears to be the prediction of the angles between the most proximal pairs of balls. Consequently, the tip error grows in proportion to the length of the robot.

Figure 7 depicts the two configurations with the largest tip position error. In Fig. 7a, a small rotation of the chain at its base would reduce the position error for all balls. In Fig. 7b, the rotational error between the first and second balls is particularly pronounced. We believe that this behavior may be due to magnetic field gradients which are not included in the model, but may be producing non-negligible forces on the balls. Nonetheless, we believe that the current model is accurate enough to use in combination with closed-loop

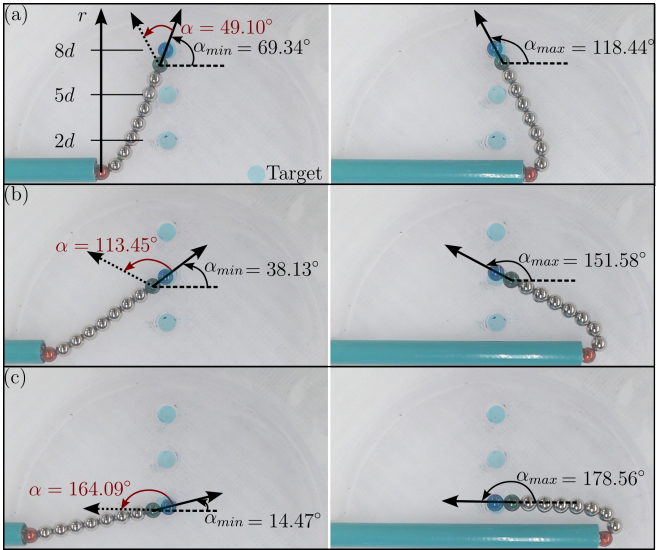


Fig. 8: Experimental analysis of the workspace for ball chain robot composed of 10 magnetic balls of  $d = 3.175$  mm diameter. Target at distance  $8d$  (a),  $5d$  (b),  $2d$  (c) from robot's axis.

control using real-time sensing.

### B. Workspace Validation

We evaluated the workspace angle of approach  $\alpha$ , as approximated in Section II and compared it with both experiment and the magnetic energy kinematic model. Three targets were used corresponding to 3 perpendicular distances from the robot axis,  $r = \{2d, 5d, 8d\} = \{6.35, 15.9, 25.4\}$  mm. For the experiments, all balls were extended from a stiff 4mm ID sheath while sheath extension and applied field direction were adjusted iteratively until the distal ball was centered in the target. This is represented in Fig. 5(c), for the intermediate target.

We measured the approach angle  $\alpha$  (see Fig. 4b) for each target, as the angle between the vector passing through the last two balls and robot's axis. The angle found experimentally is reported in Fig. 8. Note that, in the real case and the prediction of the magnetic model,  $\alpha_{max} \neq \alpha_{min}$ , which are computed independently to obtain  $\alpha$ .

We report the prediction of (17) and the magnetic model in Table I, together with the percentage error with respect to the experimental results. As expected, the error in computing the workspace with the simplified model is inversely related to the distance from the axis. In fact, as the target approaches the robot's axis,  $\alpha_{max}$  is very different from approximated value, since the chain does not form a straight line (see Fig. 8(c)). This is due to the fact that the first magnet is glued to be aligned with the main axis, offering resistance to the second ball's motion.

While, the simplified approach angle computation does overestimate the approach angle range compared to the magnetic energy model, it is a useful tool during the robot design stage since it provides an easily visualized metric for understanding the “dexterity” of the robot.

Target Distance	Experiment	Equation 17 (Error)	Magnetic Model (Error)
$8d$	$49.1^\circ$	$64.2^\circ$ (28.6 %)	$50.9^\circ$ (2.2 %)
$5d$	$113.4^\circ$	$135.8^\circ$ (19.7 %)	$120.4^\circ$ (6.1 %)
$2d$	$164.1^\circ$	$177.7^\circ$ (8.3 %)	$165.9^\circ$ (1.1 %)

TABLE I: Experimental results of workspace analysis;  $d$  diameter of the magnetic balls.

### IV. CONCLUSIONS

The present work introduces a novel approach in designing and modelling magnetic ball chain robots. This new class of robots has improved steering capabilities, when compared to other types of magnetic robot, due to the combination of discrete ball joints and high magnetic content. For this reason, it is a good candidate for steerable tip endoluminal robots.

Driven by the idea that field direction and steerable length would be primary in achieving a workspace with wider range of angles of approach, we introduced a new degree of freedom corresponding to extending the ball chain from a stiffer sheath.

With the goal of achieving motion control, we presented a kinematic model for the robot. We also derived a simplified geometric model for predicting the range of tip tangent angles which can be achieved at any tip position in the workspace and showed that the angle range is a function of the perpendicular distance from the axis of the robot.

The kinematic model is sufficiently accurate for closed-loop control when combined with sensor-based feedback. Furthermore, the approach angle estimate can serve as an efficient design tool.

### REFERENCES

- [1] P. Dupont, N. Simaan, H. Choset, and C. Rucker, “Continuum Robots for Medical Interventions,” *Proceedings of the IEEE*, 2022.
- [2] P. E. Dupont, B. J. Nelson, M. Goldfarb, B. Hannaford, A. Menciassi, M. K. O’Malley, N. Simaan, P. Valdastri, and G.-Z. Yang, “A decade retrospective of medical robotics research from 2010 to 2020,” *Science Robotics*, vol. 6, no. 60, p. eabi8017, 2021. [Online]. Available: <https://www.science.org/doi/abs/10.1126/scirobotics.abi8017>
- [3] C. Bergeles, A. H. Gosline, N. V. Vasilyev, P. J. Codd, P. J. del Nido, and P. E. Dupont, “Concentric tube robot design and optimization based on task and anatomical constraints,” *IEEE Transactions on Robotics*, vol. 31, no. 1, pp. 67–84, 2015.
- [4] G. Pittiglio, M. Mencattelli, and P. E. Dupont, “Magnetic Ball Chain Robots for Endoluminal Interventions,” 2023. [Online]. Available: [arXiv:2302.03728 \[cs.RO\]](https://arxiv.org/abs/2302.03728)
- [5] J. K.-R. Chun, S. Ernst, S. Matthews, B. Schmidt, D. Bansch, S. Boczor, A. Ujeyl, M. Antz, F. Ouyang, and K.-H. Kuck, “Remote-controlled catheter ablation of accessory pathways: results from the magnetic laboratory,” *European Heart Journal*, vol. 28, no. 2, pp. 190–195, 01 2007. [Online]. Available: <https://doi.org/10.1093/eurheartj/ehl447>
- [6] G. Pittiglio, L. Barducci, J. W. Martin, J. C. Norton, C. A. Avizzano, K. L. Obstein, and P. Valdastri, “Magnetic Levitation for Soft-Tethered Capsule Colonoscopy Actuated with a Single Permanent Magnet: A Dynamic Control Approach,” *IEEE Robotics and Automation Letters*, vol. 4, no. 2, pp. 1224–1231, 2019.
- [7] L. Barducci, G. Pittiglio, J. C. Norton, K. L. Obstein, and P. Valdastri, “Adaptive Dynamic Control for Magnetically Actuated Medical Robots,” *IEEE Robotics and Automation Letters*, vol. 4, no. 4, pp. 3633–3640, 2019.

- [8] J. Edelmann, A. J. Petruska, and B. J. Nelson, "Magnetic control of continuum devices," *International Journal of Robotics Research*, vol. 36, no. 1, pp. 68–85, 2017.
- [9] S. Jeon, A. K. Hoshiar, K. Kim, S. Lee, E. Kim, S. Lee, J.-y. Kim, B. J. Nelson, H.-J. Cha, B.-J. Yi, and H. Choi, "A Magnetically Controlled Soft Microrobot Steering a Guidewire in a Three-Dimensional Phantom Vascular Network," *Soft Robotics*, vol. 6, no. 1, pp. 54–68, 2018. [Online]. Available: <https://doi.org/10.1089/soro.2018.0019>
- [10] Y. Kim, G. A. Parada, S. Liu, and X. Zhao, "Ferromagnetic soft continuum robots," *Science Robotics*, vol. 4, no. 33, p. eaax7329, 2019. [Online]. Available: <http://robotics.sciencemag.org/content/4/33/eaax7329.abstract>
- [11] Y. Kim, E. Genevriere, P. Harker, J. Choe, M. Balicki, R. W. Regenhardt, J. E. Vranic, A. A. Dmytriw, A. B. Patel, and X. Zhao, "Telerobotic neurovascular interventions with magnetic manipulation," *Science Robotics*, vol. 7, no. 65, p. eabg9907, 2022. [Online]. Available: <https://www.science.org/doi/abs/10.1126/scirobotics.abg9907>
- [12] G. Pittiglio, P. Lloyd, T. da Veiga, O. Onaizah, C. Pompili, J. H. Chandler, and P. Valdastri, "Patient-specific magnetic catheters for atraumatic autonomous endoscopy," *Soft Robotics*, vol. 0, no. 0, p. null, 0, pMID: 35312350. [Online]. Available: <https://doi.org/10.1089/soro.2021.0090>
- [13] G. Pittiglio, M. Brockdorff, T. da Veiga, J. Davy, J. H. Chandler, and P. Valdastri, "Collaborative magnetic manipulation via two robotically actuated permanent magnets," *IEEE Transactions on Robotics*, pp. 1–12, 2022.
- [14] T. da Veiga, J. H. Chandler, P. Lloyd, G. Pittiglio, N. J. Wilkinson, A. K. Hoshiar, R. A. Harris, and P. Valdastri, "Challenges of continuum robots in clinical context: a review," *Progress in Biomedical Engineering*, vol. 2, no. 3, p. 32003, 2020. [Online]. Available: <http://dx.doi.org/10.1088/2516-1091/ab9f41>
- [15] J. J. Abbott, E. Diller, and A. J. Petruska, "Magnetic Methods in Robotics," *Annual Review of Control, Robotics, and Autonomous Systems*, vol. 3, no. 1, pp. 57–90, may 2020. [Online]. Available: <https://doi.org/10.1146/annurev-control-081219-082713>
- [16] L. Wang, D. Zheng, P. Harker, A. B. Patel, C. F. Guo, and X. Zhao, "Evolutionary design of magnetic soft continuum robots," *Proceedings of the National Academy of Sciences*, vol. 118, no. 21, p. e2021922118, 2021. [Online]. Available: <https://www.pnas.org/doi/abs/10.1073/pnas.2021922118>
- [17] A. J. Petruska and J. J. Abbott, "Optimal Permanent-Magnet Geometries for Dipole Field Approximation," *IEEE Transactions on Magnetics*, vol. 49, no. 2, pp. 811–819, 2013.